



# Pt-based alloy/carbon black nanohybrid covered with ionic liquid supramolecules as an efficient catalyst for oxygen reduction reactions

Quoc Chinh Tran<sup>a</sup>, Van-Duong Dao<sup>a</sup>, Hyun You Kim<sup>b</sup>, Kwang-Deog Jung<sup>c</sup>, Ho-Suk Choi<sup>a,\*</sup>

<sup>a</sup> Department of Chemical Engineering and Applied Chemistry, Chungnam National University, 220 Gung-dong, Yuseong-gu, Daejeon, 305-764, Republic of Korea

<sup>b</sup> Department of Materials Science and Engineering, Chungnam National University, 220 Gung-dong, Yuseong-gu, Daejeon, 305-764, Republic of Korea

<sup>c</sup> Clean Energy Research Center, Korea Institute of Science and Technology, PO Box 131, Cheongryang, Seoul 130-650, Republic of Korea



## ARTICLE INFO

### Article history:

Received 15 April 2016

Received in revised form 1 November 2016

Accepted 23 November 2016

Available online 24 November 2016

### Keywords:

Wet plasma reduction

Oxygen reduction reaction

Ionic liquid supramolecules

Trimetallic and bimetallic nanoparticles

## ABSTRACT

A facile strategy is reported for synthesizing ionic liquid supramolecules (ILSMs) as well as Pt-based alloys on the carbon black surface in a room temperature ionic liquid (1-butyl-3-methylimidazolium bis (trifluoromethylsulfonyl) imide) under one atmospheric pressure plasma. The bimetallic PtNi-nanoparticles (NPs) with a size of 2.5–3 nm are stably and uniformly hybridized on the surface of the carbon black, which is covered with a layer of ILSMs. The formation of the developed catalyst is examined using TEM, HAADF-STEM, XRD, TEM-EDS, and TGA measurements. The obtained catalyst exhibits high oxygen reduction reaction (ORR) activity, which is better than those of commercial Pt/C catalysts and Pt/C catalysts prepared without using ionic liquids. This strategy has been extended to fabricate trimetallic PtNiRu-NPs/C nanohybrids with further enhanced activities of up to 2.26 mAcm<sup>-2</sup> and 1.31 Amg<sub>Pt</sub><sup>-1</sup> at 0.9 V versus RHE. The trimetallic PtNiRu-NPs/C catalyst is also more stable than the commercial product under ORR conditions due to the chemical binding of the alloys with the carbon black and the physical stabilization of the nanohybrid materials through the conductive protecting layer of the ILSMs. The results prove that the developed catalysts push the ORR toward completion and can be a promising candidate for numerous electrocatalytic applications.

© 2016 Elsevier B.V. All rights reserved.

## 1. Introduction

Considering oxygen reductions, catalysts are the most attractive for renewable energy technologies such as fuel cells and water splitting [1–6]. Currently, carbon-supported Pt nanoparticles (NPs) are used as catalysts for oxygen reduction reactions (ORRs). However, the significant problems of Pt/C catalysts are their low durability and stability [7]. Recently, researchers have focused on the carbon-supported bimetallic alloys of Pt with transition metals (e.g. Fe, Co, Cu, Ni, Ru, etc.) due to the reduction of the d-band center and the change of Pt composition through alloying. This results in the reduction of the oxygenated chemisorb species and, subsequently, spectator species relative to those of pure Pt, thereby, enhancing the ORR activity [8–14]. Among the investigated alloy systems, the PtNi alloy is known to be a class of new catalysts with high ORR activity and is prepared through well-controlled synthesis [8,9,15].

However, drawbacks remain such as the requirement of high Pt content and insufficient durability [14,15]. Thus, the development of highly active, stable, and low-cost materials from PtNi structures remains a challenge in the current fuel cell technology.

In order to further improve the ORR activity, Pt-based trimetallic NPs have also been considered as promising catalysts [16–18]. One of the approaches to synthesizing Pt-based trimetallic NPs is alloying Pt-based bimetallic NPs with Ru. The presence of Ru not only demonstrates the further reduction of the oxygen binding energy, but also leads to increases in the adsorbed O<sub>2</sub> on the surface of trimetallic Pt-based catalysts compared with pure Pt and Pt-based bimetallic alloys, and this results in further promotion of the ORR activity [19,20]. However, the significant disadvantage of this method is the complex and ineffective route for the scalable synthesis of Pt-based trimetallic alloys.

In general, carbon-supported Pt-based alloy catalysts have been synthesized using colloidal synthesis methods with the assistance of chemical reduction agents such as hydrogen gas, LiBH<sub>4</sub>, NaBH<sub>4</sub>, ethylene glycol, alcohol, etc., as well as capping agents [4]. It should be noted that the presence of chemical reducing agents and

\* Corresponding author.

E-mail address: [hchoi@cnu.ac.kr](mailto:hchoi@cnu.ac.kr) (H.-S. Choi).

capping agents can result in numerous drawbacks in this method. For example, the chemical materials that are used may not be good for human health or the environment. Furthermore, the free access of O<sub>2</sub> to the surface of the NPs is protected by the capping agents on the surface of the NPs. Therefore, the ORR activity is decreased [21]. Thus, the development of a new method that can overcome these process restrictions is necessary. The impregnation of NPs into a hydrophobic ionic liquid could support very high activity for the ORR due to their high oxygen solubility and the protic ionic liquid [3,22–26]. The ionic liquid was impregnated into the NPs using the drop-casting method. However, this method can have numerous disadvantages such as complicated steps, non-uniform distribution of ionic liquid on the surface of NPs, and low stability of the electrode.

Recently, a new approach was developed that chemically binds Pt-NPs to multi-walled carbon nanotubes (MWNTs) in a room temperature ionic liquid (RTIL) under atmospheric pressure plasma and that physically stabilizes them through a film of ionic liquid supramolecules (ILSMs) on the surface of nanohybrid materials [27]. Most importantly, the developed materials have been applied to the generation of iodide ions from triiodide ions for use as counter electrodes in dye-sensitized solar cells and to the oxidation of methanol in the electrolyte system of 0.5 M H<sub>2</sub>SO<sub>4</sub> + 1 M CH<sub>3</sub>OH [27,28]. Furthermore, the developed technology can overcome the previously mentioned process restrictions.

The primary motivation of this study is the synthesis of Pt-based alloy/carbon black nanohybrid materials near room temperature under atmospheric pressure and their application as efficient catalysts for ORRs. For this purpose, an experimental approach was first used to simultaneously synthesize Pt-NPs and ILSMs on the carbon black surface via wet plasma reduction. The effect of the ILSMs in ORRs is examined through comparing two samples with and without ILSMs. Second, an extension of the proposed strategy to the synthesis of bimetallic PtNi-NPs and trimetallic PtNiRu-NPs on carbon black surfaces is presented. Finally, the catalytic activity of the Pt-based alloy/carbon black materials with different compositions is compared.

## 2. Experimental

### 2.1. Materials

Chloroplatinic acid hydrate (H<sub>2</sub>PtCl<sub>6</sub>·xH<sub>2</sub>O, 99.9% trace metals basis), nickel (II) chloride hexahydrate (NiCl<sub>2</sub>·6H<sub>2</sub>O, 99.999% trace metal basis), nickel (II) acetate tetrahydrate (Ni(CH<sub>3</sub>COO)<sub>2</sub>·4H<sub>2</sub>O), ruthenium (III) chloride hydrate (RuCl<sub>3</sub>·xH<sub>2</sub>O, 99.98% trace metal basis), 1-butyl-3-methylimidazolium bis(trifluoromethylsulfonyl)imide ([BMIM]TF<sub>2</sub>N), acetone, and ethanol were purchased from Sigma-Aldrich (USA). Carbon black (SuperP) was received from Graphite & Carbon Inc. (USA). Commercial Pt/C catalyst (20 wt% Pt) was obtained from Alfa Aesar (USA). The argon and hydrogen gases were purchased from Yonhap LPG (Korea). The Nafion D521 solution (5 wt%) was bought from Dupont (USA).

### 2.2. Synthesis of composite materials

In order to investigate the effect of ILSMs on the performance of the ORRs, two samples were prepared. The first sample was Pt/C prepared via dry plasma reduction (DPR) as in previous studies [29,30]. Briefly, the Pt precursor was first prepared through dissolving 10 mg of chloroplatinic acid hydrate in 2 ml of ethanol. Next, 5 mg of carbon black was dispersed on the Pt precursor solution via ultrasonication for 2 h. After that, ethanol was evaporated at 50 °C. Finally, the mixtures of Pt and carbon black in the reactor were treated with an atmospheric pressure plasma system (power:

200 W, gas flow rate: Ar–51 pm/H<sub>2</sub>–10 sccm, and treatment time: 15 min). The second sample was Pt/C prepared via wet plasma reduction as undertaken previously [27,28]. This was prepared as the first sample. However, the mixture of Pt and C was dispersed on the ionic liquid before using the plasma reduction. After the plasma treatment, the product was washed three times in acetone and then dried at 70 °C for 2 h. In order to examine the effect of the alloying transition metals with Pt on the ORR performance, two more samples (PtNi alloy/C and PtNiRu alloy/C) were prepared via wet plasma reduction. Note that the precursors used were a mixture of 10 mg of chloroplatinic acid hydrate and 10 mg of nickel (II) chloride hexahydrate in 2 ml of ethanol in order to synthesize the PtNi alloy/C and a mixture of 10 mg of chloroplatinic acid hydrate, 10 mg of nickel (II) acetate tetrahydrate, and 2 mg of ruthenium (III) chloride hydrate in 2 ml of ethanol in order to synthesize the PtNiRu alloy/C.

### 2.3. Characterization

The morphology of the synthesized composite materials was analyzed using a scanning electron microscope (SEM; JSM-7000F, JEOL, Japan). The characterization of these composites was also conducted via transmission electron microscope (TEM; JEM-2100F, JEOL, Japan). All samples dispersed in ethanol were individually dropped onto carbon-coated copper TEM grids (Ted Pella, Redding, USA) using a pipette and dried under ambient conditions. The X-ray powder diffraction (XRD) patterns were collected using an X-Pert PRO MPD high performance X-ray diffractometer with Cu-K $\alpha$  radiation (Japan). The concentration of catalysts was determined through the inductively coupled plasma-atomic emission spectroscopy (OPTIMA 7300 DV ICP-AES, USA). The weight percentages of the ILSMs bound to the surface of composite materials were determined using thermal gravimetric analysis (TGA; Mettler Toledo Inc., USA) at a heating rate of 10 °C min<sup>-1</sup> in an N<sub>2</sub> atmosphere.

### 2.4. Preparation of the working electrodes

The working electrodes were prepared on a glassy carbon rotating disk electrode (RDE) (diameter: 3 mm; area: ~0.071 cm<sup>2</sup>) from ALS Co., Ltd. (Japan). First, a homogenous solution of 50 μl of Nafion D521 solution in a 1 ml mixture of water and 2-propanol solvents with volume ratio of 3:1 was prepared using ultrasonication for 30 min. Next, 1 mg of catalysts was added and dispersed in the solution to form a homogeneous ink. The electrodes were prepared via drop-casting 3 μl of catalyst ink onto a glassy carbon electrode. Then, the samples were dried under ambient air conditions for 1 h in order to form a uniform layer. For comparison, commercial Pt/C catalysts (20 wt% Pt; Alfa Aesar, USA) were used as the reference catalysts. The reference electrode was also prepared following the same procedure as described above. The Pt loading was estimated to be 8.064 μgPt/cm<sup>2</sup>.

### 2.5. Electrochemical measurements

The characteristics of the cyclic voltammograms (CVs) were assessed using an IviumStat device. Three electrode electrochemical cells were used. A Pt mesh and Ag/AgCl (3 M Cl<sup>-</sup>) electrodes served as the counter electrode and reference electrode, respectively. Note that the reference electrode was calibrated with respect to the reversible hydrogen electrode (RHE) (Supporting information, Fig. S1). The electrochemically active surface area (EASA) measurements were conducted through CVs at room temperature in a nitrogen-saturated 0.1 M HClO<sub>4</sub> solution. The potential scan rate was 100 mV s<sup>-1</sup>. For the ORR measurements, the electrolyte was saturated with oxygen via bubbling O<sub>2</sub> for at least 30 min prior

to beginning each experiment. The disk electrode was scanned cathodically at a rate of  $5 \text{ mVs}^{-1}$ . The ORR polarization curves were obtained at a rotating speed of 1600 rpm.

### 3. Results and discussion

#### 3.1. Morphology and structure of the nanohybrid materials

##### 3.1.1. Pt-NPs/C nanohybrids

All Pt-based alloy/carbon black nanohybrids covered with ionic liquid supramolecules were prepared via simultaneous reduction of the metal precursors under the action of hydrogen radicals and electrons, which were used as reducing agents at the interface between the plasmas and ionic liquid. Similar concepts to describe the particle growth processes have been reported previously [27,28]. In particular, a schematic of the composite synthesis is presented in Fig. 1. Briefly, the metal precursors were mixed with carbon black in an ethanol solution followed by sonication for 2 h. After drying at  $50^\circ\text{C}$ , each set of mixed precursors and carbon black was dispersed on the ionic liquid. Finally, they were treated with an atmospheric pressure plasma system. The results are the formation of a Pt-based alloy immobilized on the surface of the carbon black such as Pt-IL/C, PtNi-IL/C, and PtNiRu-IL/C, which were covered with a thin layer of ILSMs as seen in the bottom panels of Fig. 1.

In order to understand the structure of the Pt-based alloy/carbon black composite, high-resolution scanning electron microscopy (HRSEM) and TEM images were obtained. As seen in Fig. 2(a), the pristine carbon black with particle size of approximately 50 nm was uniformly and clearly visible on the plane image without micropores. The Pt-NPs with very small sizes were not observed in Fig. 2(b). However, there were many pores with diameters in the range of a few to one hundred nanometers on the surface of the nanohybrid films. The results indicate that the formation of pores was primarily caused by the ILSMs: the pores were formed on the film surface as a result of the agglomeration of NPs covered with ILSMs. It should be noted that the porosity of the electrode has a significant effect on the performance of the catalyst as a result of the decrease in the resistance of the mass and charge transfers [31]. It is known that the protons can be easily conducted to the ionic liquid due to the existence of unpaired electrons on the nitrogen in the ionic liquid structure (Supporting information, Fig. S2) [3]. Furthermore, due to the perfluorinated side chains of the  $[\text{TF}_2\text{N}]$  anion in the ionic liquid structure (Supporting information, Fig. S2), the hydrophobic properties of the ionic liquid can also increase its affinity for  $\text{O}_2$  [22,23]. Thus, the formation of ILSMs has an important function in the reduction of  $\text{O}_2$ . The formation of ILSMs was confirmed using TGA analyses (Supporting information, Fig. S3) and the TEM image in Fig. 2(c). The TEM image further confirms the SEM analysis through demonstrating that a thin film of ILSMs was successfully formed on the Pt/C surface. Furthermore, as seen in Fig. 2(c), the Pt-NPs were clearly visible and successfully immobilized on the carbon black surface. The Pt-NPs were well dispersed on the carbon black surface without exhibiting agglomeration. The inset in Fig. 2(c) illustrates that the Pt-NPs had sizes in the range of 2.0–3.5 nm, but that most are 2.5 and 3 nm, which are small and highly mono-dispersed. The average size of the Pt-NPs formed without using supporters and MWNTs was 3 and 3.5 nm, respectively, as discussed previously [27,28]. However, the average size of the Pt-NPs on the carbon black was slightly smaller than those prepared without supporters and MWNTs due to the different electrostatic energy of the substrates [32]. A heavy element, i.e. Pt, is distinctly observed in the inset of Fig. 2(c), where the lattice spacing is depicted in the enlarged image, and the estimated lattice spacing was  $2.25 \text{ \AA}$ , which coincides well with Pt (111). The energy

dispersive spectroscopy (EDS), which was measured during the TEM observation, indicates that the Pt-NPs were immobilized on the carbon black surface and the Pt peaks were observed at 2.1 and  $9.6 \text{ keV}$ , as depicted in Fig. 2(d). The other peaks of C originated from the carbon black; those of O from the oxygen functional groups; those of S, N and F from the ILSMs; and those of Cu from the back grid. The results further confirmed the formation of thin film ILSMs on the surface of the nanohybrid materials. The crystal structure of the Pt-NPs was determined using XRD (Supporting information, Fig. S4). The XRD patterns of the Pt/C on the Si wafer substrate exhibited the carbon black peak at  $26.2^\circ$  and characteristic diffraction peaks of Pt (111), Pt (200), Pt (220), and Pt (311) at  $2\theta = 39.6^\circ, 45.2^\circ, 67.2^\circ$ , and  $80.7^\circ$ , respectively, which indicated that Pt was present in the face center cubic (fcc).

##### 3.1.2. Bimetallic PtNi-NPs/C nanohybrids

The TEM images of the bimetallic PtNi-NPs on the carbon black surface are presented in Fig. 3(a)–(d). The average size of the bimetallic PtNi-NPs was  $2.8 \text{ nm}$  (Fig. 3(e)), which is close to that of the Pt-NPs immobilized on the carbon black. Agglomeration of the bimetallic NPs was not found on the carbon black surface, as seen in Fig. 3(a) and (b). Therefore, in order to obtain further understanding of the effect of the supporter, the bimetallic PtNi-NPs were synthesized without using supporters. The results are presented in Fig. S5 (Supporting information). Spherical PtNi-NPs with sizes of 2–4 nm were obtained; however, they tended to agglomerate. This result indicates that the carbon supporter is critical for the growth of highly dispersed alloy PtNi [33]. Fig. 3(c) depicts clear lattice fringes with a lattice spacing of  $2.21 \text{ \AA}$ , which corresponds to the {111} plane of an fcc  $\text{Pt}_2\text{Ni}$ . The EDS (Supporting information, Fig. S6), which was measured during the TEM observation, identified the bimetallic PtNi-NPs immobilized on the carbon black surface. The formation of the alloy PtNi on the carbon black was examined using XRD measurements (Supporting information, Fig. S6). The thin film of the ILSMs was clearly observed in Fig. 3(d). This result was further confirmed using TGA analyses (Supporting information, Fig. S3). In order to obtain more information about the elemental distribution in the bimetallic PtNi-NPs, high-angle annular dark field-scanning transmission electron microscopy-energy dispersive spectroscopy (HAADF-STEM-EDS) measurements were performed. As seen in Fig. 3(f) and (g), the cross-sectional compositional line profile revealed a bimetallic alloy structure characterized by the homogeneous distribution of the Pt and Ni in a single NP. The ICP-AES exhibited a Pt:Ni ratio of  $66:34 \approx 2:1$  (Supporting information, Table S1), while the Pt:Ni ratio in the starting materials was 1:5. The difference in the Pt/Ni element ratio between the starting material and product could be attributed to the difficulty in reducing Ni(II)/Ni in the current system and the strong tendency of Ni to be alloyed with Pt [34,35].

##### 3.1.3. Trimetallic PtNiRu-NPs/C nanohybrids

The extension of the proposed strategy to the synthesis of trimetallic PtNiRu NPs on the carbon black surface is discussed here. The preparation of trimetallic PtNiRu-NPs/C is similar to the synthesis of bimetallic PtNi-NPs/C nanohybrids, except for the introduction of an additional 2 mg of  $\text{RuCl}_3$  in the reaction solution. The morphology of the trimetallic PtNiRu-NPs/C is illustrated in Fig. 4(a)–(c). As seen in the figures, trimetallic PtNiRu-NPs with irregular shapes were uniformly distributed and firmly immobilized on the carbon black surface. More NPs were agglomerated compared with the Pt-NPs/C NPs. The particle size of the trimetallic PtNiRu-NPs was in the range of 2–4 nm and was typically 3 nm (Fig. 4(d)), which was slightly larger than those of the Pt-NPs and bimetallic PtNi-NPs on the carbon black surface. The difference in the electrostatic energies of the various alloy NPs with substrates could be regarded as an explanation of this result [32,36].

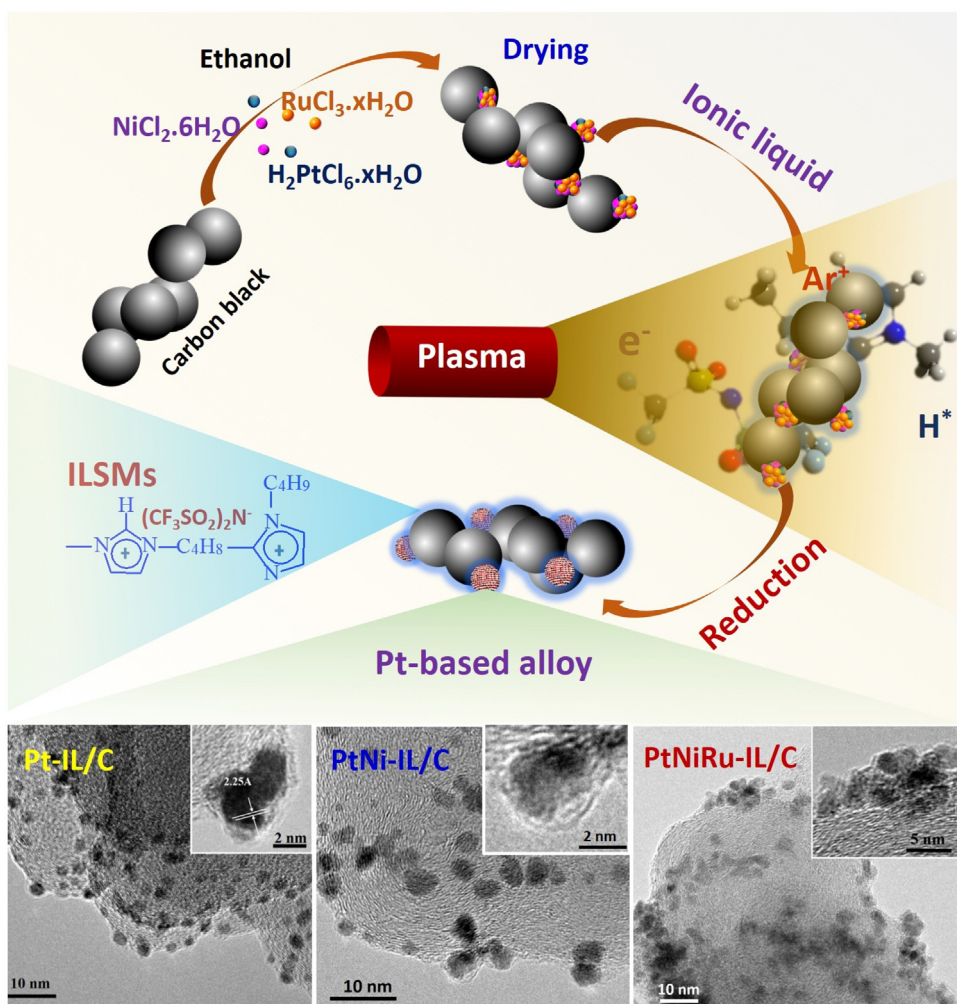


**Fig. 1.** Schematic of the process of synthesizing the Pt-based alloy/carbon black nanohybrid covered with ionic liquid supramolecules (ILSMs) using wet plasma reduction. The bottom of the figure depicts the HR-TEM images of the Pt-IL/C, PtNi-IL/C, and PtNiRu-IL/C composites, respectively.

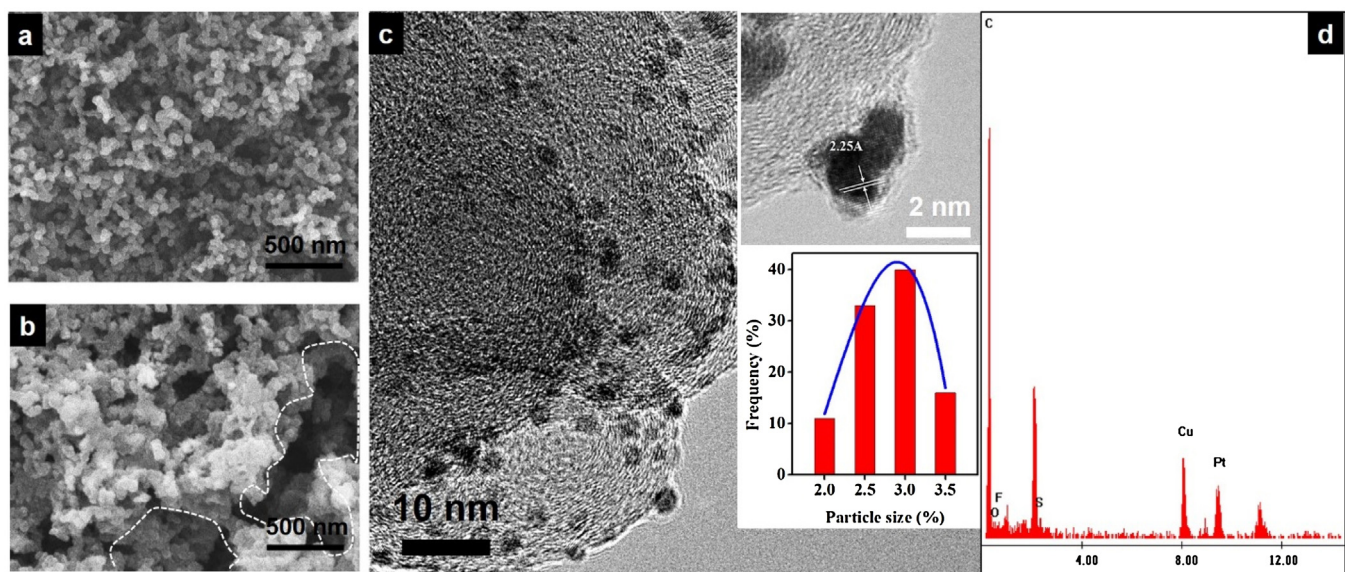


**Fig. 2.** (a) HRSEM plane image of pristine carbon black; (b) HRSEM plane image of Pt/C; (c) TEM image indicating the Pt-NPs immobilized on the carbon black surface; the insets of (c) present the TEM images with lattice spacings and particle size distributions of the Pt-NPs attached to the carbon black; and (d) EDS spectra obtained from the total area of the TEM image in (c).

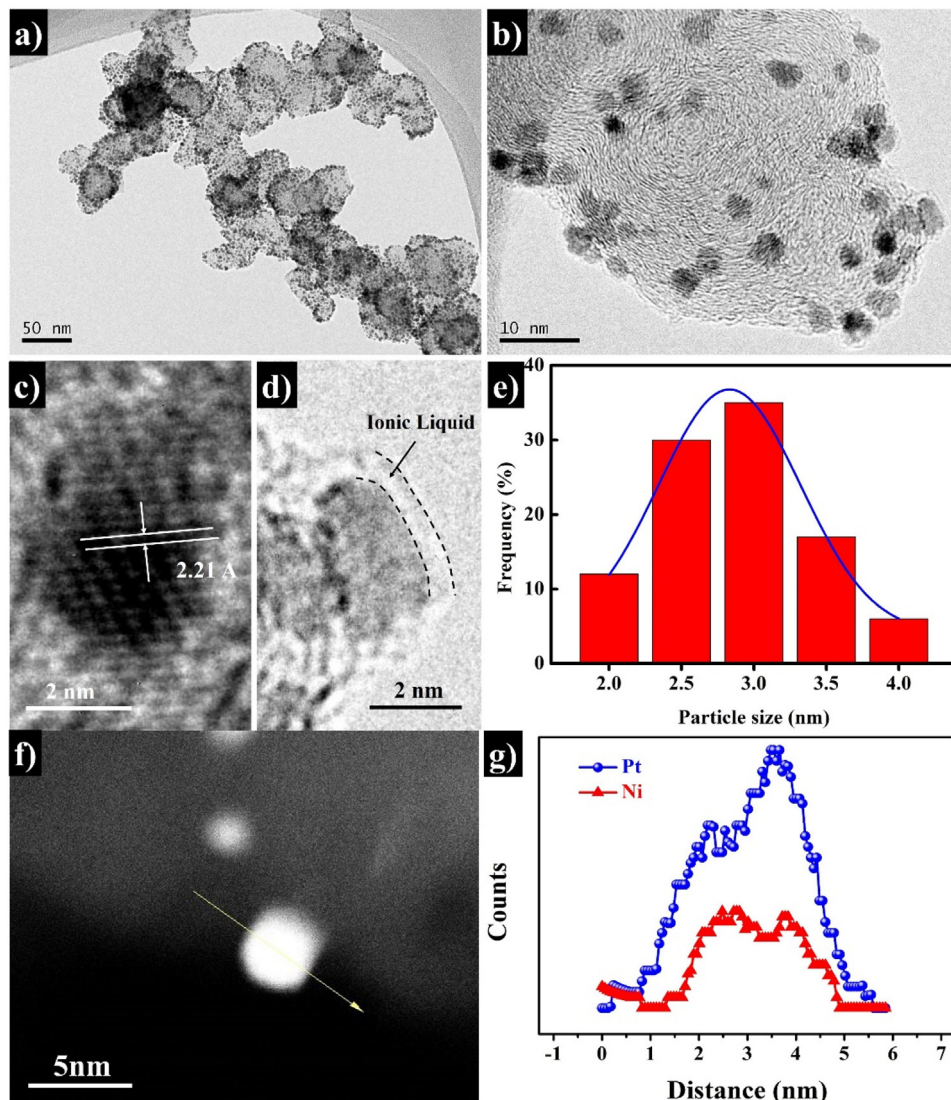


**Fig. 3.** (a-d) TEM images of PtNi-alloy/C with different scale bars; (e) particle size distribution of the PtNi-NPs obtained from 400 randomly selected particles from (a); (f) HAADF-STEM-EDS image of PtNi-alloy/C; and (g) cross-sectional compositional line profile of the bimetallic PtNi-NPs.

**Fig. 4(b)** presents the spacing of the adjacent fringes, which was approximately  $2.21\text{ \AA}$  and is close to that of the (111) plane of the  $\text{Pt}_2\text{Ni}$  alloy ( $2.21\text{ \AA}$ ). The thin film of ILSMs on the surface of the nanohybrid material was also observed in **Fig. 4(c)**; this was further confirmed via TGA analysis in Fig. S3 (Supporting information). In order to determine the molar ratio in the trimetallic NPs, ICP-AES was conducted. The ICP-AES data determined that the molar ratio of Pt:Ni:Ru was 59:26:15, which is denoted here as  $\text{Pt}_2\text{Ni}_1\text{Ru}_{0.5}$  (Supporting information, Table S1). The alloy structure of the trimetallic PtNiRu-NPs was further confirmed through linear scans of the electron energy loss spectroscopy (EELS) with a higher spatial resolution across on a single NP, as depicted in **Fig. 4(e)**. As seen in the figure, the individual Pt, Ni, and Ru elements were distributed evenly in the nanocrystal. This demonstrates that the PtNiRu alloy/C nanohybrid was successfully synthesized using the wet plasma reduction. The result is in good agreement with the XRD analyses in Fig. S7 (Supporting information).

### 3.2. Catalytic activity of the nanohybrid materials

The electrocatalytic performances of the developed nanohybrid materials were evaluated through comparative analyses of the CVs.

The five electrodes were prepared and tested as working electrodes. There were three electrodes fabricated from Pt-based ILSMs/C, which are denoted as Pt-IL/C, PtNi-IL/C, and PtNiRu-IL/C. The commercial Pt/C (20 wt% Pt, Alfa Aesar, USA) was used as a reference for comparison, and it is denoted c-Pt/C. In order to estimate the effect of the ILSMs, the Pt/C nanohybrid was prepared using a dry plasma reduction without using ionic liquid [29], which is denoted as Pt/C. The morphology and structure of Pt/C are presented in Fig. S8(a). Therefore, the structure of Pt/C was not covered by ILSMs, as seen in Fig. S8(b), and this was further confirmed through the absence of S and F element peaks, which resulted from the ILSMs in the TEM-EDX spectra (Fig. S8(c)).

#### 3.2.1. Electrochemically active surface area

**Fig. 5(a)** presents the CVs with different working electrodes. As seen in the figure, the initiation potential of the Pt oxidation was 0.88 V for c-Pt/C, while the values of 0.92, 0.95, 0.962, and 0.965 V were obtained for Pt/C, Pt-IL/C, PtNi-IL/C, and PtNiRu-IL/C, respectively. Overall, the difference in the Pt oxidation peaks was not significant for Pt-IL/C, PtNi-IL/C, and PtNiRu-IL/C. However, the developed catalysts, which were covered by ILSMs on the surface, had a higher potential of Pt oxidation peaks than the commercial

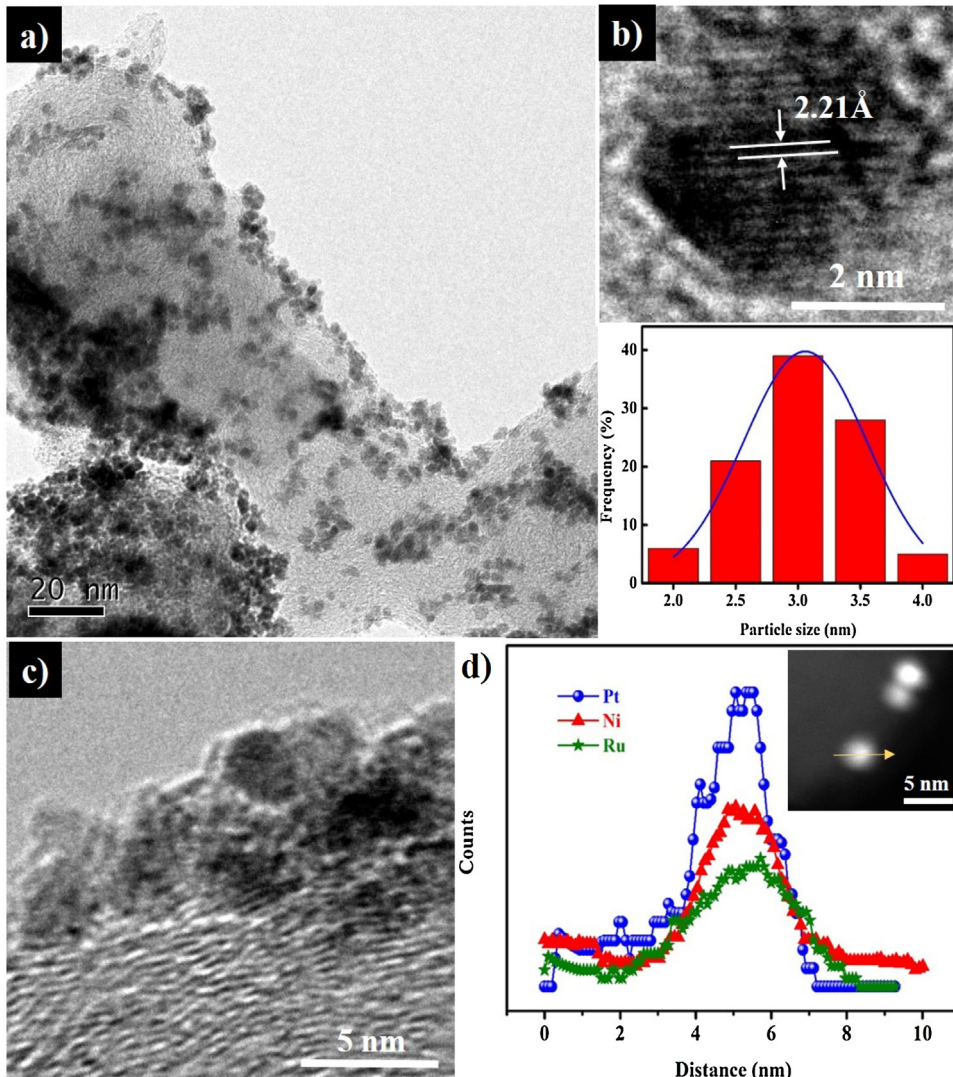


**Fig. 4.** (a–c) TEM images of PtNiRu-alloy/C with different scale bars; (d) particle size distribution of the PtNiRu-NPs obtained from 400 randomly selected particles from (a); (e) cross-sectional compositional line profile of the trimetallic PtNiRu-NPs, with the inset depicting the HAADF-STEM-EDS image of PtNiRu-alloy/C.

catalyst and the catalyst prepared without ionic liquid. It is well known that increases in the potential of Pt oxidation are related to the suppression of Pt oxide formation, which results in the improvement of the ORR activity due to the decrease in the active site blocking  $\text{OH}_{\text{ad}}$  species. These results indicate that the formation of ILSMs on the catalyst surfaces has an important function in suppressing the Pt oxide formation and enhancing the ORR activity.

Next, the electrochemically active surface area (EASA) of the catalysts was estimated using the CV measurements. The results are presented in Fig. 5(b). As seen in the figure, the hydrogen adsorption/desorption peaks appeared in the potential range of 0.075–0.4 V. The EASA values were 62.5, 59.6, 63.4, and  $60.9 \text{ m}^2 \text{ g}^{-1}$  for Pt/C, Pt-IL/C, PtNi-IL/C, and PtNiRu-IL/C, respectively. They were slightly smaller than  $64.9 \text{ m}^2 \text{ g}^{-1}$  for c-Pt/C. All values were within  $\pm 5\%$  of the average EASA. The comparison of the EASA values for different electrodes is presented in Fig. 5(b).

### 3.2.2. Electrocatalytic performances

The ORR was measured in  $\text{O}_2$ -saturated 0.1 M  $\text{HClO}_4$  solutions at room temperature with a sweep rate of  $10 \text{ mV s}^{-1}$ . The ORR polarization curves with various catalysts are presented in Fig. 5(c). As

seen in the figure, there were two distinguishable potential regions: the first was the diffusion-limited current region below 0.6 V and the second was the mixed kinetic-diffusion controlled region in the range of 0.7–1.0 V.

Fig. 5(c) clearly demonstrates that the ORR activity of Pt/C was lower than that of Pt-IL/C. Furthermore, the ORR activity of PtNi-IL/C was higher than that of Pt-IL/C, while it was lower than that of PtNiRu-IL/C. The results demonstrate that the ORR activity was strongly dependent on the formation of ILSMs on the catalyst surface as well as the catalyst compositions. Fig. 5(c) also demonstrates that the ORR activity of the developed catalysts was higher than that of c-Pt/C. From Fig. 5(c), it was also found that the diffusion-limited current densities of the electrodes were similar for the samples under investigation. However, the overpotential for ORR decreased in the following order: PtNiRu-IL/C < PtNi-IL/C < Pt-IL/C < Pt/C < c-Pt/C. Note that the values were compared with 1.2 V for the standard reaction potential. It is well known that decreases in the overpotential for ORR indicates increases in activity for ORR. Thus, the developed catalysts exhibited higher activity than the commercial product.

The mass and area specific activities of the catalysts were calculated from the ORR polarization curves. The mass-transport

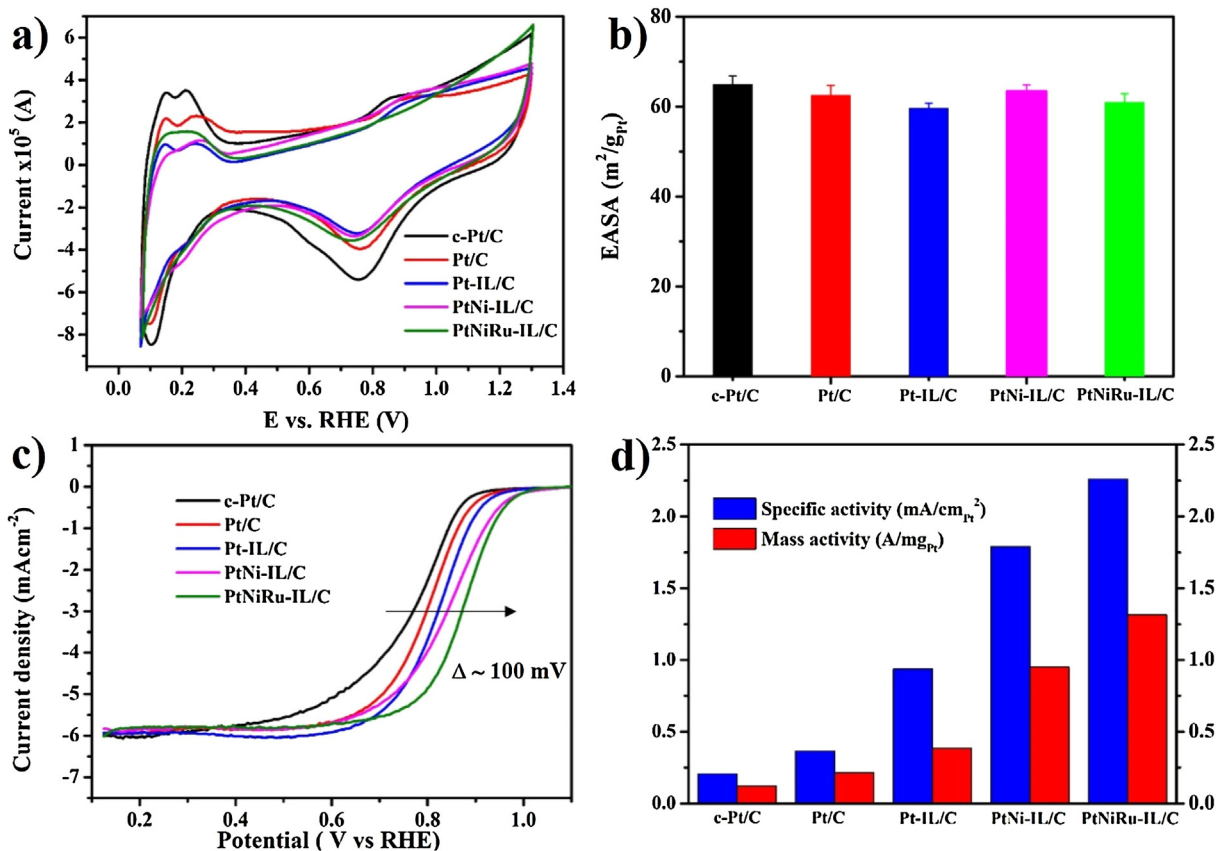


**Fig. 5.** (a) CVs recorded for different catalysts in 0.1 M HClO<sub>4</sub> solution; (b) EASA of the catalysts; (c) ORR polarization curves for various catalysts; and (d) mass activity and specific activity at 0.9 V (vs. RHE) for these three catalysts.

correction was used according to the Koutecky-Levich equation:  $I_k(A) = I_{lim}(A)*I(A)/(I_m - I)$ , where  $I_k$  is the kinetic current (A) and  $I_m$  is the diffusion-limited current [37,38]. The activity of the catalysts was estimated via normalization of the kinetic current for both the EASA and the amount of Pt loading. Note that the  $I$  value is normally calculated at  $E = 0.90$  V and the  $I_{lim}$  value is obtained at 0.40 V versus a reversible hydrogen electrode. The results are depicted in Fig. 5(d).

First, the effect of the Pt size on the mass activity and specific activity of catalysts is discussed. As depicted in Fig. 5(d), the mass activity and specific activity for Pt/C were  $0.22 \text{ Amg}_{\text{Pt}}^{-1}$  and  $0.37 \text{ mAcm}^{-2}$ , respectively, which were 1.83 times and 1.76 times higher than that of the c-Pt/C catalyst. The difference in the size of Pt-NPs on the carbon black surface could be a significant reason for this result. Furthermore, the size of the Pt on the commercial product was 5 nm, which is larger than the 3 nm for Pt on the Pt/C, as depicted in Fig. S8 (Supporting information). This is consistent with the better surface accessibility of the Pt/C catalyst synthesized in this study. As discussed above, the Pt-NPs synthesized using the DPR method were not only uniform with a small size of approximately 3 nm, but were also well distributed on the carbon black surface with a high number density of Pt-NPs, but without aggregation.

Second, the effect of the ILSMs on the electrocatalytic performance for ORR is examined. In order to achieve this purpose, the performances of the Pt/C and Pt-IL/C catalysts were compared. The results are also presented in Fig. 5(d). As seen in the figure, the mass and specific activities of the Pt-IL/C catalyst were  $0.39 \text{ Amg}_{\text{Pt}}^{-1}$  and  $0.94 \text{ mAcm}^{-2}$ , respectively. Both parameters were higher than  $0.22 \text{ A.mg}_{\text{Pt}}^{-1}$  and  $0.37 \text{ mAcm}^{-2}$  for the Pt/C catalyst. These results are in good agreement with previous publications [26,39]. The

Pt-NPs in both Pt/C and Pt-IL/C catalysts had similar sizes, shapes, and Pt loadings. Therefore, an increase in the activity of the Pt-IL/C catalyst must result from the ILSMs. To further demonstrate the effect of ILSMs on the electrocatalytic performance for ORR, we compared the ORR activities of Pt-based alloys incorporated with ILSMs to Pt-based alloys without ILSMs, as shown in Table S2. Table S2 highlighted that Pt-based alloys incorporated with ILSMs showed better ORR activities than those of Pt-based alloys without ILSMs. Two factors contributed to the improvement of activity in the Pt-based alloy-IL/C catalyst. The first factor was the increase in the oxygen solubility due to the formation of the ILSMs. It is known that the structure of ILSMs is composed of ionic liquid components [27]. The oxygen solubility of the protic ionic liquid was  $8.37 \pm 0.05 \text{ mM}$  for [BMIM]TFSI, which was 6.9 times higher than that of the dilute aqueous HClO<sub>4</sub> ( $1.21 \pm 0.05 \text{ mM}$ ) [22,40]. Facile oxygen supply through the ILSMs to the Pt nanoparticle would significantly improve the sluggish ORR kinetics. The second factor for the increasing activity of Pt-IL/C was its ability to control the ILSM protons [17] due to the generation of protons through free electrons in the nitrogen of the imidazolium cation. In addition, the suppression of the Pt oxidation potential was also assigned to the improved ORR activity in the composite catalyst, as discussed above. These results are consistent with other previous reports [26,39].

Finally, a comparative study of the electrochemical performance was conducted using different alloy structures for the ORR. For this purpose, a set of Pt-IL/C, PtNi-IL/C, and PtNiRu-IL/C was fabricated and tested. The results are presented in Fig. 5(c) and (d). As seen in the figures, the mass activity of  $0.95 \text{ Amg}_{\text{Pt}}^{-1}$  and specific activity of  $1.79 \text{ mAcm}^{-2}$  were found for PtNi-IL/C at 0.9 V (vs. RHE). These values were better than those for Pt-IL/C. Interestingly, the highest values for both the mass activity and specific activity were

**Table 1**

Comparison of ORR activities for different catalysts in the same measurement conditions (\*).

Catalyst	Mass activity ( $\text{Amg}^{-1}$ )	Specific activity ( $\text{mAcm}^{-2}$ )	References
PtPdRu dendrites	1.25	1.65	[18]
PtPdRu dendritic nanocages	2.61	2.90	[18]
FePtCu nanorods	0.22	0.30	[41]
PtPdBi nanowires	1.16	1.48	[42]
PtPdBi nanospheres	0.67	1.12	[42]
Pt-IL/C composite	0.39	0.94	This study
PtNi-IL/C composite	0.95	1.79	This study
PtNiRu-IL/C composite	1.31	2.26	This study

\* Specific and mass activity numbers of the catalysts were measured at room temperature in  $\text{O}_2$ -saturated 0.1 M  $\text{HClO}_4$  with a sweep rate of  $10 \text{ mVs}^{-1}$  and a rotation rate of 1600 rpm.

achieved with the PtNiRu-IL/C catalyst. That is, as seen in Fig. 5(d), the mass and specific activities of PtNiRu-IL/C were  $1.31 \text{ AmgPt}^{-1}$  and  $2.26 \text{ mAcm}^{-2}$ , respectively. These values were approximately 10.8 times higher than those of the c-Pt/C catalysts. It should be noted that the mass activity of PtNiRu-IL/C was also higher than that of  $1.25 \text{ Amg}^{-1}$  for the PtPdRu nanodendrites,  $0.22 \text{ Amg}^{-1}$  for PtFeCu nanorods,  $1.16 \text{ Amg}^{-1}$  for PtPdBi nanowires, and  $0.67 \text{ Amg}^{-1}$  for PtPdBi nanosphere catalysts under experimental conditions similar to those used in this study, as described in Table 1 [18,41,42]. Due to the similarity in size, shape, metal loading, and ILSMs immobilized on the catalyst surfaces, it can be concluded that the enhancement of the electrochemical performance with different alloy structures for ORR is assigned to the critical role of composition.

$\text{Pt}_3\text{Ni}(111)$  and Pt-Ni octahedral nanoparticles have been reported as a more reactive catalyst for ORR than conventional Pt catalysts [21]. Ni was found to be distributed across the outermost layers, and the unique electronic structure of the Pt–Ni ensemble depressed the surface concentration of the –OH related species [43–45]. It should be noted that Ru can also contribute to further improve the interaction between Pt and other metals. In order to prove this point, XPS measurements were conducted. The results are presented in Fig. S9. As depicted in Fig. S9, the binding energy of Pt  $4f_{7/2}$  gradually increased for the different Pt-based alloys in the following order: Pt < PtNi < PtNiRu. It is given that the increase in the binding energy Pt  $4f_{7/2}$  core level referred to the reduction of the surface d-band center at the transition metal surface [45,46]. Moreover, the surface d-band center has an important function in controlling the ORR activity [44]. Therefore, the second metal (Ni, or especially Ru) alloyed with Pt induces an increase in the binding energy of the Pt core states. Therefore, the decrease of the d-band state results in a decrease in the metal-O bonding strength (as well as the metal-OH bonding) and, subsequently, improvement in the ORR kinetics [44]. In contrast, according to Brimaud et al., the  $\text{Pt}_x\text{Ru}_{3-x}$  local surface ensembles bind  $\text{OH}_{ad}$  species more weakly than the  $\text{Pt}_3$  trimer [19]. Thus, the  $\text{OH}_{ad}$  binding energy of the Pt-rich mixed trimers (Pt<sub>3</sub>Ru) are expected to be weaker than that of Pt(111); consequently, these surfaces could exceed Pt(111) in ORR activity [19]. The synergistic ligand effects of Pt-Ru [11] and Pt-Ni [21,43–45] increase the surface coverage of oxygen and lower that of  $\text{OH}_{ad}$  and other poisoning/spectating species. Thus, a combination of the geometric ensemble effects and lateral ligand effects in the Pt-Ru system reduced the overpotential for PtNiRu-IL/C in comparison with that of Pt-IL/C and PtNi-IL/C [19]. Together with the facile oxygen supply from the covering ILSMs, the optimized binding nature of the developed PtNiRu-IL/C catalyst leads to its improved ORR activity. Note that the molar ratio of Pt, Ni, and Ru in the PtNiRu-IL/C was 59:26:15, which is a Pt-rich surface alloy ( $\text{Pt}_2\text{Ni}_1\text{Ru}_{0.5}$ ). Therefore, the PtNiRu-IL/C catalyst

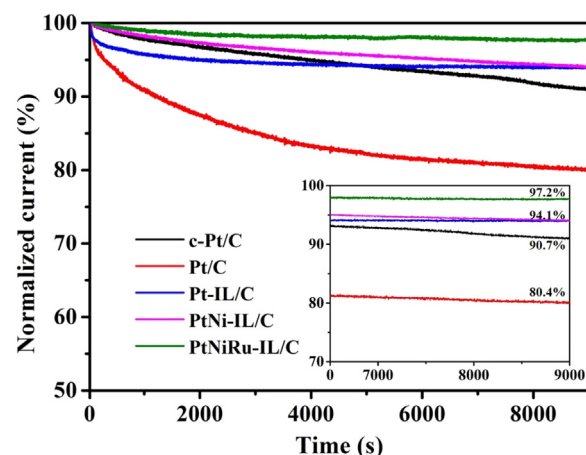


**Fig. 6.** Chronoamperometric response (percentage of current retained vs. operation time) for different electrodes at 0.7 V (vs. RHE) in an  $\text{O}_2$  saturated electrolyte.

might be regarded as one with Pt-rich surface compositions for the improvement of ORR catalytic activity [17,47].

### 3.2.3. Electrochemical durability

In order to investigate the electrochemical durability of the catalysts toward ORRs, chronoamperometric tests were conducted for the c-Pt/C, Pt/C, Pt-IL/C, PtNi-IL/C, and PtNiRu-IL/C electrodes at 0.7 V in  $\text{O}_2$ -saturated 0.1 M  $\text{HClO}_4$ . The results are presented in Fig. 6. It was found that the developed catalysts had better durability than that of the c-Pt/C catalyst: 6.1% of the ORR activity was reduced for Pt-IL/C during operation for 9000 s, while the c-Pt/C was 9.3%. The PtNi-IL/C showed a 5.9% loss and PtNiRu-IL/C exhibited superior durability with only a 2.8% loss for 9000 s. Compared to Pt-IL/C, PtNi-IL/C and PtNiRu-IL/C showed better stability. The distinctive long-term stability of the catalysts synthesized in this study is highly promising as it assures the consistency of the catalyst under operation. It is assumed that the ILSMs layer and the alloyed Ni, Ru synergistically contribute to the improved stability of the PtNiRu-IL/C catalyst. Alloying Pt with Ni, Ru alters electronic structures of Pt, resulting in the reduction of the binding energies for oxygen species onto PtNi, PtNiRu-IL/C, and thus improves the poison tolerance [48,49]. While as, the ILSMs layer can physically protect metal nanoparticles and thus prevent the catalyst deactivation upon the agglomeration. Furthermore, the hydrophobic ILSMs at the PtNiRu-IL/C catalyst surface also prevent the dissolution of the metal nanoparticles (Pt, Ru, Ni) to acidic electrolyte through effectively pushing water molecules away from the surface [26]. It was further demonstrated by the 19.6% loss of the ORR activity for Pt/C catalysts, which were not incorporated with ILSMs layer, during operation for 9000 s. On the other hand, Ru could strengthen the catalyst-C interaction and anchor metal nanoparticles to the support. Moreover, Ru at the surface of the catalyst can preferentially bind the reaction spectators or deactivators such as CO and –OH as reported in the Pt-Ru core-shell catalyst for the preferential oxidation of CO in hydrogen [48]. In this regard, Ru secures more active sites on the catalyst surface and improves the activity and stability simultaneously. Further delicate catalyst optimizations such as Au pairing [50] could maximize the consistency of the developed PtNiRu-IL/C catalyst. Overall, the developed catalysts outperformed the superior ORR activity compared with the c-Pt/C due to the physical stabilization of the NPs through the conductive protective layer of ILSMs, as well as the chemical binding between the carbon black and NPs [27].

## 4. Conclusion

Pt-based alloys dispersed on carbon black impregnated with ILSMs were synthesized under one atmospheric pressure plasma. The Pt and Pt-based alloys were successfully immobilized on the carbon black surface with particle sizes in the range of 2.5–3 nm. The nanohybrid materials were covered by ILSMs, which were formed during the plasma reduction. The formation of the alloy structure was confirmed using TEM, HAADF-STEM-EDS, EELS, and XRD. The long-term stability of the developed catalysts for electrochemical durability of the ORR was clearly improved through the chemical binding of the alloys with carbon black and the physical stabilization of the nanohybrid materials through the conductive protecting layer of ILSMs. The electrocatalytic performances demonstrated that the mass activity ( $1.31 \text{ Amg}_{\text{Pt}}^{-1}$ ) and specific activity ( $2.26 \text{ mAcm}^{-2}$ ) of the PtNiRu-IL/C catalyst were approximately 10.8 times higher than those of the c-Pt/C catalysts. Thus, it is expected that the developed materials, which exhibit long-term stability as well as excellent specific and mass activity for ORR with small amounts of Pt, can be robust and low-cost catalysts for fuel cells and electrocatalytic applications.

## Acknowledgements

This research was supported by a National Research Foundation (NRF) grant (2014R1A2A2A01006994), the Korea Research Fellowship Program (2015H1D3A1061830), and a Korea CCS R&D Center (KCRC) grant (2014M1A8A1049345). These are all funded by the Ministry of Science, ICT and Future Planning through the National Research Foundation of Korea.

## Appendix A. Supplementary data

Supplementary data associated with this article can be found, in the online version, at <http://dx.doi.org/10.1016/j.apcatb.2016.11.051>.

## References

- [1] I. Dumitrescu, R.M. Crooks, PNAS 109 (2012) 11493–11497.
- [2] Y. Chen, J. Xu, X. Liu, Y. Tang, T. Lu, Appl. Catal. B: Environ. 140–141 (2013) 552–558.
- [3] A. Khan, X. Lu, L. Aldous, C. Zhao, J. Phys. Chem. C 117 (2013) 18334–18342.
- [4] R. Bashyam, P. Zelenay, Nature 443 (2006) 63–66.
- [5] T.H. Yu, T. Hofmann, Y. Sha, B.V. Merinov, D.J. Myers, C. Heske, W.A. Goddard III, J. Phys. Chem. C 117 (2013) 26598–26607.
- [6] Y. Liang, Y. Li, H. Wang, J. Zhou, J. Wang, T. Regier, H. Dai, Nat. Mater. 10 (2011) 780–786.
- [7] D. Sebastián, A.G. Ruiz, I. Suelves, R. Moliner, M.J. Lázaro, V. Baglio, A. Stassi, A.S. Aricó, Appl. Catal. B: Environ. 115–116 (2012) 269–275.
- [8] (a) D.A. Cantane, F.E.R. Oliveira, S.F. Santos, F.H.B. Lima, Appl. Catal. B: Environ. 136–137 (2013) 351–360;  
 (b) D.Y. Chung, S.W. Jun, G. Yoon, S.G. Kwon, D.Y. Shin, P. Seo, J.M. Yoo, H. Shin, Y.-S. Chung, H. Kim, B.S. Mun, K.-S Lee, N.-S. Lee, S.J. Yoo, D.-H. Lim, K. Kang, Y.-E. Sung, T. Hyeon, J. Am. Chem. Soc. 137 (49) (2015) 15478–15485.
- [9] C.H. Cui, L. Gan, M. Neumann, M. Heggen, B.R. Cuenya, P. Strasser, J. Am. Chem. Soc. 136 (2014) 4813–4816.
- [10] L. Yang, M.B. Vukmirovic, D. Su, K. Sasaki, J. Herron, M. Mavrikakis, S. Liao, R.R. Adzic, J. Phys. Chem. C 117 (2013) 1748–1753.
- [11] R. Loukrakpam, J. Luo, T. He, Y. Chen, Z. Xu, P.N. Njoki, B.N. Wanjala, B. Fang, D. Mott, J. Yin, J. Klar, B. Powell, C.-J. Zhong, J. Phys. Chem. C 115 (5) (2011) 1682–1694.
- [12] (a) A. Jackson, V. Viswanathan, A.J. Forman, A.H. Larsen, J.K. Nørskov, T.F. Jarillo, ChemElectroChem 1 (2014) 67–71;  
 (b) W. Alammari, M. Govindhan, A. Chen, ChemElectroChem 2 (2015) 2041–2047.
- [13] S. Brimaud, A.K. Engstfeld, O.B. Alves, H.E. Hoster, R.J. Behm, Top. Catal. 57 (2014) 222–235.
- [14] L. Gan, M. Heggen, S. Rudi, P. Strasser, Nano Lett. 12 (2012) 5423–5430.
- [15] L. Zou, J. Fan, Y. Zhou, C. Wang, J. Li, Z. Zou, H. Yang, Nano Res. 8 (2015) 2777–2788.
- [16] (a) S. Zhang, S. Guo, H. Zhu, D. Su, S. Sun, J. Am. Chem. Soc. 134 (2012) 5060–5063;  
 (b) P. Mani, R. Srivastava, P. Strasser, J. Power Sources 196 (2011) 666–673.
- [17] K. Eid, V. Malgras, P. He, K. Wang, A. Aldalbahi, S.M. Alshehri, Y. Yamauchi, L. Wang, RSC Adv. 5 (2015) 31147–31152.
- [18] K. Eid, H. Wang, V. Malgras, Z.A. Alothan, Y. Yamauchi, L. Wang, J. Phys. Chem. C 119 (2015) 19947–19953.
- [19] U.A. Paulus, A. Wokaun, G.G. Scherer, T.J. Schmidt, V. Stamenkovic, N.M. Markovic, P.N. Ross, Electrochim. Acta 47 (2002) 3787–3798.
- [20] M.K. Bede, Nature 486 (2012) 43–51.
- [21] (a) C.H. Cui, L. Gan, H.H. Li, S.H. Yu, M. Heggen, P. Strasser, Nano Lett. 12 (2012) 5885;  
 (b) C.H. Cui, L. Gan, M. Heggen, S. Rudi, P. Strasser, Nat. Mater. 12 (2013) 765.
- [22] J. Snyder, T. Fujita, M.W. Chen, J. Erlebacher, Nat. Mater. 9 (2010) 904–907.
- [23] L. Johnson, A. Ejigu, P. Licence, D.A. Walsh, J. Phys. Chem. C 116 (2012) 18048–18056.
- [24] E. Benn, H. Uvegi, J. Erlebacher, J. Electrochem. Soc. 162 (2015) H759–H766.
- [25] C. Ke, J. Li, X. Li, Z. Shao, B. Yi, RSC Adv. 2 (2012) 8953–8956.
- [26] J. Snyder, K. Livi, J. Erlebacher, Adv. Funct. Mater. 23 (2013) 5494–5501.
- [27] V.D. Dao, S.H. Ko, H.S. Choi, J.-K. Lee, J. Mater. Chem. 22 (2012) 14023–14029.
- [28] Q.C. Tran, V.-D. Dao, K.-D. Jung, H.-S. Choi, Electrochim. Acta 143 (2014) 357–365.
- [29] V.D. Dao, Q.C. Tran, S.H. Ko, H.S. Choi, J. Mater. Chem. A 1 (2013) 4436–4443.
- [30] V.D. Dao, H.S. Choi, Chem. Commun. 49 (2013) 8910–8912.
- [31] Y.-H. Cho, H.-S. Park, Y.-H. Cho, D.-S. Jung, H.-Y. Park, Y.-E. Sung, J. Power Sources 172 (2007) 89–93.
- [32] Z. Luo, L.A. Somers, Y. Dan, T. Ly, N.J. Kybert, E.J. Mele, A.T.C. Johnson, Nano Lett. 10 (2010) 777–781.
- [33] X.Q. Huang, Z.P. Zhao, Y. Chen, E.B. Zhu, M.F. Li, X.F. Duan, Y. Huang, Energy Environ. Sci. 7 (2014) 2957–2962.
- [34] J. Zhang, H.Z. Yang, J.Y. Fang, S.Z. Zou, Nano Lett. 10 (2010) 638–644.
- [35] T.C. Deivaraj, W.X. Chen, J.Y. Lee, J. Mater. Chem. 13 (2003) 2555–2560.
- [36] V.D. Dao, L.V. Nang, E.T. Kim, J.K. Lee, H.S. Choi, ChemSusChem 6 (2013) 136–1319.
- [37] Y. Garsany, O.A. Baturina, K.E. Swider-Lyons, Anal. Chem. 82 (2010) 6321–6328.
- [38] B. Lim, M. Jiang, P.H.C. Camargo, E.C. Cho, J. Tao, X. Lu, Y. Zhu, Y. Xia, Science 324 (2009) 1302–1305.
- [39] C. Chen, Y. Kang, Z. Huo, Z. Zhu, W. Huang, H.L. Xin, J.D. Snyder, D. Li, J.A. Herron, M. Mavrikakis, M. Chi, K.L. More, Y. Li, N.M. Markovic, G.A. Somorjai, P. Yang, V.R. Stamenkovic, Science 343 (2014) 1339–1343.
- [40] I. Bahadur, K. Osman, C. Coquelet, P. Naidoo, J. Phys. Chem. B 119 (2015) 1503–1514.
- [41] H. Zhu, S. Zhang, S. Guo, D. Su, S. Sun, J. Am. Chem. Soc. 135 (2013) 7130–7133.
- [42] H. Liao, Y. Hou, Chem. Mater. 25 (2013) 457–465.
- [43] V.R. Stamenkovic, B. Fowler, B.S. Mun, G.F. Wang, P.N. Ross, C.A. Lucas, N.M. Markovic, Science 315 (2007) 493–497.
- [44] V.R. Stamenkovic, B.S. Mun, K.J.J. Mayrhofer, P.N. Ross, N.M. Markovic, J. Rossmeisl, J. Greeley, J.K. Norskov, Angew. Chem. Int. Ed. 45 (2006) 2897–2901.
- [45] C. Wang, M. Chi, D. Li, D. Strmcnik, D. van der Vliet, G. Wang, V. Komanický, K.-C. Chang, A.P. Paulikas, D. Tripkovic, J. Pearson, K.L. More, N.M. Markovic, V.R. Stamenkovic, J. Am. Chem. Soc. 133 (2011) 14396–14403.
- [46] M.V. Ganduglia-Pirovano, V. Natoli, M.H. Cohen, J. Kudrnovsky, I. Turek, Phys. Rev. B: Condens. Matter Mater. Phys. 54 (1996) 8892–8898.
- [47] S.W. Yoon, V.D. Dao, L.L. Larina, J.K. Lee, H.S. Choi, Carbon 96 (2016) 229–236.
- [48] S. Alayoglu, A.U. Nilekar, M. Mavrikakis, B. Eichhorn, Nat. Mater. 7 (2008) 333–338.
- [49] H. Zhang, M. Jin, J. Wang, M. Kim, D. Yang, Y. Xia, J. Am. Chem. Soc. 13 (2011) 10422–10425.
- [50] J. Zhang, K. Sasaki, E. Sutter, R.R. Adzic, Science 315 (2007) 220–222.